Nuclear Instruments and Methods in Physics Research B 328 (2014) 48–58

Contents lists available at ScienceDirect

Nuclear Instruments and Methods in Physics Research B

journal homepage: www.elsevier.com/locate/nimb

Mössbauer Magnetic Scan experiments

G.A. Pasquevich [a,b,d,*], P. Mendoza Zélis [a,b,,d], A. Lencina [a,c], A. Veiga [b,d], M.B. Fernández van Raap [a,b], F.H. Sánchez [a,b]

[a] Departamento de Física, Facultad de Ciencias Exactas, Universidad Nacional de La Plata, P.O. Box 67, 1900 La Plata, Argentina
[b] Instituto de Física La Plata, CONICET, P.O. Box 67, 1900 La Plata, Argentina
[c] Centro de Investigaciones Ópticas (CONICET La Plata – CIC), P.O. Box 3, 1897 Gonnet, Argentina
[d] Facultad de Ingeniería, Universidad Nacional de La Plata, P.O. Box 91, 1900 La Plata, Argentina

ARTICLE INFO

Article history:
Received 10 July 2013
Received in revised form 14 February 2014
Accepted 20 February 2014

Keywords:
Mössbauer Magnetic Scans
Constant velocity mode
Magnetic domains
Magnetic moment orientations distribution
Site specificity

ABSTRACT

We report an application of the Mössbauer Effect designed to retrieve specific information on the magnetic response of iron-containing materials. It consists in the measurement of the nuclear absorption of gamma-rays as a function of an external magnetic field for a specific nuclear transition between magnetically-split nuclear levels. The experiments, here termed Mössbauer Magnetic Scan experiments, were carried out recording the absorption of ^{57}Fe 14.4 keV gamma-ray in α-Fe at constant Doppler energies coincident with some of the spectral lines of the magnetically split Mössbauer spectrum. Due to the dependence of the transition probabilities on the relative orientation between the nuclear magnetic moment and the gamma-ray direction, the present application results in a useful method to study the magnetic-field evolution of the distribution of atomic-magnetic-moment orientations. The proposed technique inherit from the Mössbauer Spectroscopy the chemical-element selectiveness as well as the ability to differentiate responses from iron atoms located at inequivalent site or at different phases.

In this work, we show that the data analysis for these experiments depends on the sample thickness that the gamma-ray has to cross. For thin samples (i.e.samples with Mössbauer effective thicknesses lower than one) the magnetic-field dependence of the second-order-moment of the orientation distribution in the direction of the gamma ray is obtained. On the other hand, for thicker samples, although the data analysis is more complex, the dependences of the three second-order-moments of the orientation distribution are obtained.

The experiments were performed on two α-Fe foils of different Mössbauer effective thicknesses. They were chosen to represent the cases of thin and thick Mössbauer absorbers. The magnetic evolution of the orientations distribution is compared with results obtained from magnetometric measurements showing a good agreement as well indicating the complementarity of both techniques.

A complete description of the experimental set up and the formalism for Mössbauer Magnetic Scan data analysis are presented.

1. Introduction

Experimental methods measuring site-specific magnetic responses represent a basic and technological need in today's scientific world. The magnetic response of multiphase magnetic materials and of single-phase crystalline materials with nonequivalent magnetic atoms is of particular interest. This response either from different phases or from different structural sites of one particular phase of the materials to static and dynamic fields is a key point to understand the effect of local interactions in material properties. Single-phase nanomaterials, for instance, show that the magnetic response of spins in free surfaces and other interfaces is markedly different from that of spins in bulk regions. This is so due to the different atomic configurations and coordinations in the different locations.

Among others, some synchrotron techniques are selective to chemical elements and provide local information. X-ray Magnetic Circular Dichroism [1] has the property of being able to discern between the contributions to total magnetization of different atomic species present in a complex sample [2]. However, in cases in which the same element is located at non equivalent sites, for

* Corresponding author at: Departamento de Física, Facultad de Ciencias Exactas, Universidad Nacional de La Plata, P.O. Box 67, 1900 La Plata, Argentina. Tel.: +54 2214246062.
E-mail address: gpasquev@fisica.unlp.edu.ar (G.A. Pasquevich).

http://dx.doi.org/10.1016/j.nimb.2014.02.118
0168-583X/

example Fe in magnetite, the dichroism signal is an average over these sites. Indeed, the problem on how the atomic magnetic-moments, located at octahedral and tetrahedral sites in this compound, individually respond to an applied magnetic field has been addressed by a more sophisticated synchrotron technique: site-specific diffraction anomalous near-edge structure [3]. This advantageous type of observation is not provided by most commonly used magnetometric techniques, which frequently give only information on the average magnetic moment component in one space direction. Therefore, the development of new, low cost, experimental methods and equipments with such ability is highly desirable.

Mössbauer Effect Spectroscopy is a widely used technique to study condensed matter [4,5]. It is a chemical-element selective technique and has the ability to distinguish probes in different phases or sites. Nowadays this spectroscopy is applied in a variety of disciplines [6], for example nano-science, biology, mineralogy, archeology, corrosion, solid state physics, to mention just a few. In the magnetic study of iron-containing alloys, this spectroscopy stands out due to its ability to fully characterize magnetic fields in internal domains. Besides, its high energy resolution allows to distinguish probes at inequivalent sites.

Another use of the Mössbauer effect comprises the measurement of gamma-ray resonant absorption as a function of some parameter (e.g. temperature, pressure, degree of advance of a reaction) at a constant Doppler energy. Detailed information about physical dependences on such parameters can be retrieved by this kind of experiments. This idea was used in several works where the energy was fixed at the centroid of the Mössbauer effect spectrum and the temperature was swept with the aim of determining characteristic temperatures (e.g. Curie temperature [7], crystallization on-set temperature [8], magnetic order temperature [8]). It was also applied to kinetic studies of phase transformations in which reaction rates were not slow enough to be accurately observed by Mössbauer spectroscopy. For example, selectiveness was essential to study recombination kinetics of the photodissociated Myglobin-CO [9] and nanocrystallization of $Fe_{73.5}Si_{13.5}Cu_1Nb_3B_9$ amorphous alloy [10]. More recently, we reported on some conceptual and practical advances of this approach accomplished by a set of experiments in which the Doppler energy was fixed at various values [11], or varied following a feedback [12] or a preset protocol, while the temperature was being changed. It was demonstrated that this method provides a higher degree of detail on material transformations than that obtained from the measurement of a limited number of conventional spectra.

Recently, the focus of our work has been extended to retrieve information of magnetic materials and their responses to applied magnetic fields. The methodology relies on the measurement of the resonant absorption of gamma-rays at fixed Doppler energies as a function of a magnetic field. In this case, a change in the relative intensities of the absorption lines is expected. This change is due to the nuclear-transition probability dependence on the angle between the nuclear magnetic-moment and the gamma-ray direction [4,5]. By selecting the Doppler energy coincident with one absorption maximum, the dependence of the magnetic-moment orientation on the applied magnetic field can be inferred.

In a previous work we have termed this kind of experiments as Mössbauer Magnetic Scan (MMS) experiments [13]. There, taking advantage of the tunability and selectivity of the technique, independent responses of the ^{57}Fe atomic magnetic-moments located at the nanocrystalline and amorphous phases of a nanocrystallized $Fe_{90}Zr_7B_3$ sample were observed. Distinctive features were found on each scan, according to the spectral line and structural phase to which they belonged. But it was not possible to explain the scans by using the thin absorber approximation formalism [14], not even qualitatively. Here, thin and thick mentions are related to the effective Mössbauer absorber thickness t, given by [14],

$$t = \sigma_0 f_A n d, \tag{1}$$

where σ_0 is the maximum nuclear resonance absorption cross section, f_A is the recoil-free fraction, n the number of Mössbauer isotopes (in this case ^{57}Fe) per unit volume and d the sample thickness. Then, thin and thick absorbers correspond to effective thickness lower and greater than the unit, respectively. The main analysis difference between thin and thick absorbers, relies on the dependence of the spectral shape on the effective thickness. For thin absorbers, the absorption spectral function results linear in t, i.e. the line intensities and the spectral area are proportional to t, retaining the spectral shape. This linear behavior is not present in the case of thick absorbers [14–16]. As a consequence, thin absorber spectral analysis results more reliable. In fact, the linearity allows the decomposition of the spectrum in sum of sub-spectra and the quality of the information retrieved from the spectral line positions and their relative intensities does not depend on thickness accuracy.

Although the thin absorber formalism is widely used to analyze Mössbauer spectra even for samples with $t \approx 1$ [17], it does not account for changes in gamma-rays polarization as they travel through the sample. Indeed, for thick absorbers this fact usually cannot be ignored. Gonser et al. [16,18] observed significant changes in Mössbauer spectra in very thick samples (even remarkable changes as the apparition of additional absorption lines) that were evidently related with the polarization that the incident unpolarized beam acquires into the sample. Although for intermediate thickness the polarization effects are not reflected in the Mössbauer spectra line positions, this effect is clearly reflected in the spectral line intensities. Since MMS experiments focus on the line intensities, for a proper analysis, gamma-ray polarization process must be considered. To take into account these effects, we have extended the formalism introduced by Hirvonen et al. [19] and Daniels [20].

In this work, a thorough understanding of the MMS technique is accomplished. Their fundamentals and experimental details are described. Moreover, the mathematical procedure to properly analyze a given MMS curve is developed. The technique is tested with two α-Fe foils of 1 μm (thin) and 13 μm (thick), associated with effective Mössbauer thicknesses smaller and larger than one, respectively. It is confirmed that thick absorber MMS curves can only be analyzed under a formalism that jointly considers thickness and polarization effects. Besides, unlike the thin absorber case, information about the atomic magnetic-moment components orthogonal to the gamma-ray direction can be recovered.

2. Fundamentals

In this section, the underlying physics supporting the basic assumptions of MMS technique is described. The major relation that has to be discussed is the one between the direction of the atomic magnetic moment **m** and the spectral line intensities. Although there is an evident and direct relation between these intensities and the nuclear magnetic moment $\mathbf{m}_n$, the usefulness of the present application on condensed-matter-magnetism issue is more conditioned to a good understanding of the connection of spectral line intensities with atomic-magnetic-moment orientations. In this regard, a huge amount of interesting cases provides solid arguments holding a parallelism between the nuclear and the atomic magnetic moments. Here we put together these ideas and arguments because they are needed to interpretate the present methodology and also serve as a starting point to extend the interpretation to those cases in which this parallelism is not ensured.

Since the 14.4 keV nuclear transitions of ^{57}Fe nuclide is primarily magnetic-dipole type [4], their probabilities depend on the relative directions of the absorbed photon (γ) wave-vector and the nuclear magnetic moment. Therefore the spectral line intensities store information on this relative orientation. The link between the orientations of $\mathbf{m}$ and $\mathbf{m}_n$ is mainly given by the Hyperfine interaction, more specifically by the magnetic Hyperfine interaction and the Hyperfine Field $\mathbf{B}_{hf}$. We shall limit the analysis to cases in which the hyperfine interaction is purely magnetic. In such cases the $\mathbf{m}_n$ orientation is parallel (or anti-parallel) to the magnetic induction field at the nuclear site $\mathbf{B}_{eff} = \mathbf{B}_{ext} + \mathbf{B}_{hf}$; where $\mathbf{B}_{ext}$ is the external magnetic induction field. Thus the relation between the atomic magnetic moment and the $\mathbf{B}_{eff}$ stores the relative orientation between both magnetic moments.

Usually $\mathbf{B}_{hf}$ is much larger than $\mathbf{B}_{ext}$ (for example $\mathbf{B}_{hf} = 33$ T for α-Fe at room temperature and is much larger than commonly used *dc*-fields). Hence, in what follow we shall assume $\mathbf{B}_{eff} \approx \mathbf{B}_{hf}$. The Hyperfine field, in α-Fe and in most of the magnetic-metallic-iron-containing alloys, is proportional to the average atomic spin sensed by the nucleus $\langle \mathbf{S} \rangle_n$ [5]. Although inner *s*-shells of iron are completed, a non vanishing $\langle \mathbf{S} \rangle_n$ value arises from a difference in the radial distribution of the wave functions associated of electrons with different spin polarization [4,5,21]. This induced polarization at the nucleus site is promoted, due to exchange interactions, by the spin-imbalance of the outer valence 3*d*-shells, which are related to the atomic (or ionic) magnetism. In fact, the direction of $\langle \mathbf{S} \rangle_n$ is anti-parallel to the net valence spin direction [21]. Since these electronic spins define the atomic (or ionic) magnetic moment (specially in transition metals where the orbital angular momentum is quenched by the crystalline field), we can conclude that $\mathbf{B}_{hf}$ direction coincides with the direction of the atomic magnetic-moment.

The Zeeman interaction between $\mathbf{B}_{eff}$ and $\mathbf{m}_n$ splits the nuclear energy levels. When transitions between ground-state sublevels $I = 1/2$ and excited-state $I = 3/2$ of the 14.4 keV-^{57}Fe-nuclear-magnetic-dipole is considered, the Zeeman interaction combined with the selection rules allows only six transitions. Moreover, owing the magnetic dipole nature of these transitions, their probabilities depend on the angle θ between nuclear magnetic-moment and the γ direction.

Mössbauer Effect Spectroscopy is a technique that allows to measure energy and intensity of some nuclear transitions. Energy resolution is very high and close to the intrinsic natural line width of the nuclear levels, e.g. 9 neV for ^{57}Fe 14.4 keV transition. It is based on the phenomenon, know as Mössbauer Effect, of the emission and resonant absorption of gamma-ray photons without nuclear recoil and without thermal broadening [4]. The ^{57}Fe Mössbauer spectrum associated with the situation described in the previous paragraph displays six lines symmetrically arranged around an energy denoted as the isomer shift. In this case, the lines are labeled from $i = 1$ to 6 for increasing energy and they are characterized by intensities L_i and linewidths Γ_i. The Mössbauer spectrum dependence on $\mathbf{B}_{eff}$ can be summarized by two main features: the lines positions are related to $\mathbf{B}_{eff}$ magnitude while the line intensities depend on $\mathbf{B}_{eff}$ orientation respect to gamma-ray direction.

In a macroscopic ferromagnetic sample the atomic magnetic-moments are organized in microscopic domains and, within each domain, they are aligned to each other. In such systems a weak applied magnetic field $\mathbf{H}$ is enough to change the domain structure and consequently the distribution of the atomic magnetic-moment orientations. Therefore, a weak $\mathbf{H}$ could generate a significant change in the distribution of $\mathbf{B}_{eff}$ orientations without a substantial change on its magnitude.

The heretofore mentioned ideas, allow us to state that in ferromagnetic samples containing Mössbauer probes, an applied magnetic field that modifies the atomic magnetic-moment distribution, changes its Mössbauer spectrum in two ways: the position of the lines shift and their relative intensity vary (several previous works have used these facts to obtain information on the distribution of nuclear magnetic-moments orientations, usually termed spin texture, from a set of Mössbauer spectra [22–24]). A continuous dependence of the atomic magnetic-moment distribution on $\mathbf{H}$ can be obtained from the measurement of the line intensities as a function of this field. If the line shift is negligible compared to the linewidth, a scan of the γ-absorption by Mössbauer effect at fixed energy coincident with one of the nuclear transitions, gives the dependence of the line intensity with $\mathbf{H}$ within a good approximation.

As an example, let us consider a thin α-Fe sheet having an uniform distribution of magnetic-moment orientations. The Mössbauer spectrum consist of six absorption lines with relative intensities 3:2:1:1:2:3 [25,15,4]. When a magnetic field is applied, the lines shift and their intensities change. The absorption at a *fix energy* is affected due to both phenomena. For metallic iron, an applied field of 80 kA/m (parallel to the sheet) is enough to reach a high magnetization state, leading an important change in the magnetic-moments orientations and eventually a significant change in the line intensities. If total magnetic saturation is assumed, the relative line intensities become 3:4:1:1:4:3. Since the spectral area remains invariant, a change of 25% in the Mössbauer line intensity of the first and sixth line is produced. On the other hand, these lines (the external) are the most shifted due to the presence of the magnetic field. Their shift is 0.084 times their full width at half maximum (assumed 0.2 mm/s). This shift would be manifested as an absorption change (at a fixed energy coincident with the line center) of only 2.5%. Therefore there is at least one order of magnitude between both effects. The shift effect should be lesser for the inner lines, and even lesser for lower fields. Thus, for such low fields over soft magnetic samples, the dependence of the Mössbauer transmission at a fixed energy might be interpreted as a direct observation of the orientation distribution of atomic magnetic-moments.

3. Experimental

3.1. Methodology

A MMS experiment is the measurement of the gamma-ray transmission at a fixed Doppler energy as a function of an external magnetic field. The transmission is measured in the same way as in conventional Mössbauer Effect Spectroscopy, i.e. using a gamma counting system consisting of a proportional counter, a preamplifier, a pulse-shaping amplifier and a single channel analyzer [5]. The gamma-ray energy is fixed using a constant-velocity strategy [26], which is adjusted to match the nuclear transition under study. This energy can be determined from a conventional spectrum of the sample.

While the Doppler energy of the gamma rays is kept at a single value, the magnetic field is driven by a periodic signal synchronized with the channel advance of a Multichannel Scaler that records transmission. This is the same strategy used to synchronize Doppler velocity and acquisition in Mössbauer Effect Spectroscopy, therefore the same instrumentation can be used for this purpose.

Normalization of MMS curves to background transmission must be performed for quantitative data analysis. To that end, the mean transmission rate (r_{MMS}) was measured at the MMS experiment energy and at a background energy (r_{bkg}), i.e. at an energy where no resonance occurs, during a short period of time under the periodic external field. Relative-to-background MMS curves are obtained by multiplying the raw curves by a factor that assures a mean value coincident with r_{MMS}/r_{bkg}.

3.2. Experimental details

Two α-Fe foils of thicknesses of 1 μm and 13 μm were measured and analyzed. They correspond to Mössbauer effective thicknesses t of $0.5f_A$ and $6.0f_A$ respectively. The former was made by sputtering an iron target over a Kapton substrate at around 373 K. The latter was a commercial Mössbauer calibration foil.

Mössbauer spectra and MMS curves were measured with an unpolarized ^{57}Co(*Rh*) source of about 50 mCi under transmission geometry. Instrumentation consists of ORTEC pulse processing modules (142PC, 572A and 551-TSCA), Nucleus MCS-II multichannel scaler and CMTE MA-250 linear velocity transducer with MR-350 drive.

A constant velocity module (see Fig. 1) [26,27] was used to provide the velocity reference for the electromechanical transducer in place of the Multichannel Scaler used in traditional experiments, leaving the latter to drive the magnetic field. The constant-velocity module provides a smooth shaped constant velocity reference with programmable return trajectory and a digital output for external synchronization (*enable* in Fig. 1).

The constant velocity strategy has an inherent dead time, necessary to move the source backward within its periodic movement with null mean displacement. Available *enable* logic signal is routed to an AND gate in order to discard nuclear events occurring during return path. In this way the pulses recorded by the Multichannel Scaler are strictly related to the velocity under study.

Special care must be taken on the selection of the operating frequencies (Multichannel Scaler and constant velocity module) to avoid the appearance of interference patterns (Moiré patterns).

The frequency of the constant velocity reference was selected at 10 Hz after testing the optimal transducer response. A backward trajectory of 20% of the period was selected. Considering an additional 5% for stabilization of the constant velocity regime, a 75% net counting time (duty cycle) was obtained.

MMS curves of both samples were acquired at fixed Doppler velocities relative to metallic iron isomer shift: −0.84(2), 3.07(2) and 5.30(2) mm/s. They correspond to the mean velocity position of the absorption lines 3, 5 and 6 during a magnetic field period.

The magnetic field was either generated with a custom electromagnet or a pair of Helmholtz coils. High-amplitude magnetic field experiments were performed with the former and high field precision experiments (but of lower amplitude) with the latter. The electromagnet was built up from an Iron-Silicon transformer nucleus with a rectangular transverse section of 32×26 mm^2, where a core-gap of 26 mm was cut off. It was wound with 500 turns of Cu wire so that when fed with 1 A, a magnetic field of 33 kA/m were obtained at the center of the core-gap. The maximum applied current was 3.6 A, which produced 120 kA/m at the sample position. A maximum 6% deviation from linearity was observed in the field/current ratio. The custom Helmholtz coils were built with a mean diameter of 10 cm and 350 turns per coil, producing a 4.8 kA/m field with 1 A current.

An electromagnet driver, based on National LM4780 audio power amplifier, was designed to feed the magnetic field transducer with a current proportional to the triangular output voltage of the Multichannel Scaler. For that purpose a small resistor (Rs) in series with the coil is used to provide current (i.e. H) feedback. The Multichannel Scaler was set at 4096 channels and swept at 2 ms per channel (dwell time) in order to obtain a low frequency of 0.122 Hz. The relation between MMS channel number and applied magnetic field was determined using a Hall probe TMAG-01T-R from GlobalMag.

MMS experiments were carried out using a triangular wave as current reference for the magnetic transducer. Therefore, two equivalent MMS curves are obtained, one for the upward ramp and other for the downward ramp. Both curves match and data presented here are an average of these two curves. In all the performed scans a completely good overlapping was observed.

The samples were oriented perpendicular to the gamma-ray beam and parallel to the direction of the applied magnetic field (Fig. 2). Under this geometry the applied field tends to align the magnetic-moments perpendicular to the gamma-ray beam.

Standard magnetic characterization of the two foils was achieved using a VSM LakeShore 7404 vibrating sample magnetometer under the same geometry of MMS experiments. First, cycles were registered operating the magnetometer with maximum applied field 90 kA/m. Then cycles were measured with a maximum field of 760 kA/m to obtain the saturation magnetization M_s. To this end, a theoretical expression discussed in Ref. [28, p. 198] was fitted to the asymptotic behavior of M vs. H.

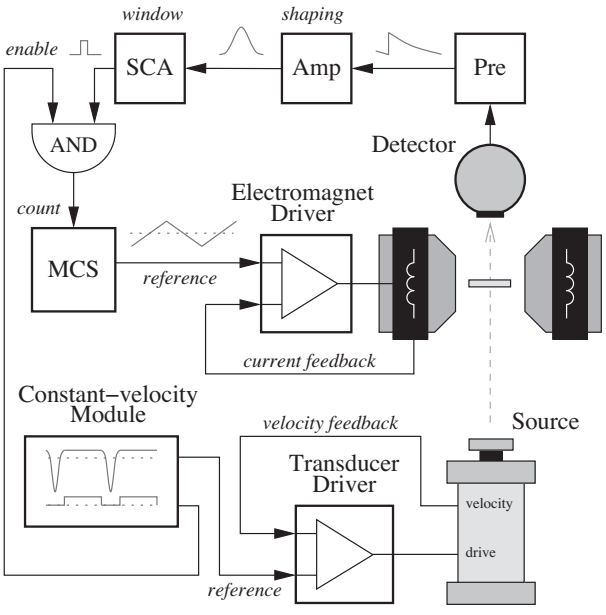

Fig. 1. Outline of the experimental setup for MMS experiments. The characteristics of the individual modules are described in the text. Pre: pre-amplifier, Amp: pulse shape amplifier, SCA: single channel analyzer, MCS: multichannel scaler.

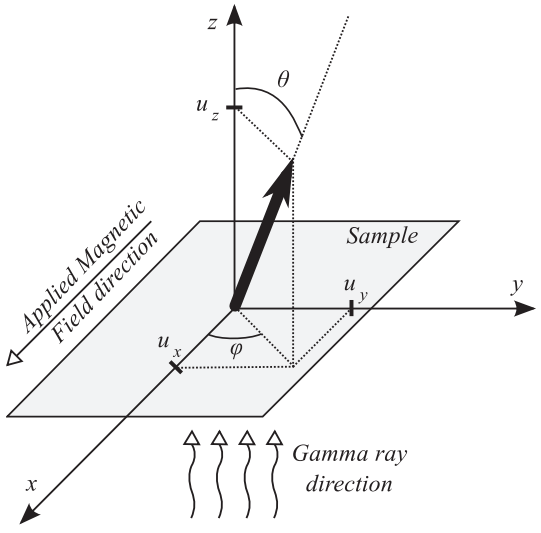

Fig. 2. Axis selection for the analysis of the experiments. The sample is located on the x-y plane and the gamma-ray beam travels in the z-direction, while the external magnetic field is applied on the x-direction.

The low-amplitude magnetic field MMS results for the 1 μm sample were compared with M vs. H curves acquired under the same conditions of MMS experiments. To this end sample foil was placed into a small and flat 200-turns sensing coil, and precisely positioned in the Helmholtz coils, in the same place as in the MMS experiments. The sensing coil was connected in series to a second coil with opposite winding, and carefully located in a position where the induced *e.m.f.* in absence of sample was zero. The *e.m.f.* was recorded with a digital Tektronix TDS3012–100 MHz oscilloscope and numerically integrated to achieve the M vs. H curve. To ensure a good induced signal in M vs. H recordings, these experiments were made at 100 Hz.

4. Results

The selected velocities to perform the scans at lines 3, 5 and 6 of the spectrum are indicated by arrows in Fig. 3(a) and (b) where the Mössbauer spectra of both samples are shown. Fig. 3(c) and (d) show the positive velocity part of the Mössbauer spectra of both samples with and without applied field. As can be noted, the presence of the magnetic field is mostly reflected in the variation of the line's relative intensity. The scans carried out at the velocities of lines 3, 5 and 6 are shown in Fig. 3(e) and (f) for both samples.

The MMS curves are smooth with a singularity near zero field. As happens on the low branch of a hysteresis loop, the recordings on the negative half of the H axis correspond to the demagnetization process, while those on the positive half correspond to the magnetization one. There is an evident slope discontinuity at the transition between these two process (demagnetization and magnetization).

MMS curves of both samples display several common features. The major variations appear in the low field region, while in the high field region the changes are smoother revealing the closeness to magnetic saturation. However, both samples have distinctive behaviors, particularly on the fifth line MMS curve (see Fig. 3(e) and (f)). In the next sections we will show that these differences in the field dependence are related to the Mössbauer effective thicknesses of the samples and the polarization process of the gamma-ray.

4.1. Thin absorber

In the thin absorber limit the line intensity depends on the angle θ between the directions of the gamma-ray beam and the nuclear magnetic-moment [4,5]. If the sample presents a distribution of magnetic-moment orientations, the intensity L_i of each line is proportional to the corresponding mean transition probability p_i,

$$p_1(u_z) = p_6(u_z) = \frac{3}{16}(1 + \langle u_z^2 \rangle), \tag{2a}$$

$$p_2(u_z) = p_5(u_z) = \frac{1}{4}(1 - \langle u_z^2 \rangle), \tag{2b}$$

$$p_3(u_z) = p_4(u_z) = \frac{1}{16}(1 + \langle u_z^2 \rangle), \tag{2c}$$

where $\hat{\mathbf{u}} = (u_x, u_y, u_z)$ is a unit vector in the direction of the atomic magnetic-moment (see Fig. 2) and $\langle \cdots \rangle$ stands for the arithmetic mean over the whole sample.

Within this framework, it is possible to explain the shape of the thin sample MMS curves (Fig. 3(e)). When the magnetization is forced into the sample plane, $\langle u_z^2 \rangle \to 0$, then p_5 should tend to its maximum value as the experimental results shows. Furthermore, the lines 3 and 6 decrease its intensities in concordance with the corresponding expressions. The mean value of u_z^2 can be isolated from Eq. (2) as a function of the relative intensities L_{56} of lines 5 to 6 as

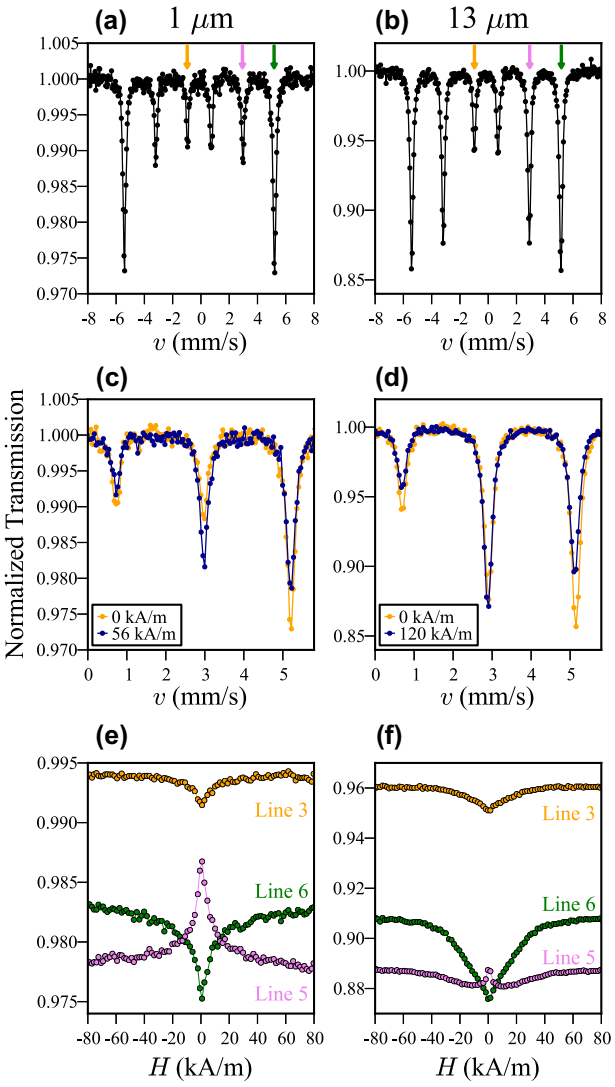

Fig. 3. (a) 1 μm and (b) 13 μm samples Mössbauer spectra in absence of applied magnetic field. The arrows indicate Doppler velocities chosen to make the Mössbauer Magnetic Scans (−0.84(2), 3.07(2) and 5.30(2) mm/s relative to metallic iron isomer shift). (c) and (d) Comparison of the positive velocity side of the spectra with and without applied magnetic field for the 1 μm and 13 μm sample respectively. (e) and (f) Mössbauer Magnetic Scans performed at the indicated absorption lines on the 1 μm and 13 μm sample respectively.

$$\langle u_z^2 \rangle = \frac{4 - 3L_{56}}{4 + 3L_{56}}. \tag{3}$$

This mean value is the u_z-second-order-moment of the orientation distribution. If mirror symmetry respect to the sample plane is assumed, $\langle u_z^2 \rangle$ can be interpreted as the variance of u_z, and can be used as a measure of the dispersion of z projection component.

The $\langle u_z^2 \rangle$ dependence on the applied magnetic field derived through Eq. 3 for the thin sample is shown in Fig. 4(a). At the highest negative field the sample presents an almost in-plane magnetic-moment distribution ($\langle u_z^2 \rangle \approx 0$). As the field intensity decreases $\langle u_z^2 \rangle$ grows (i.e. the dispersion grows), revealing a demagnetization process in which the out-of-plane projection of the magnetic-moments rises. This growth occurs until the field reaches a characteristic value in which an apparent maximum appears in $\langle u_z^2 \rangle$ (indicating a maximum dispersion). We define this magnetic field as the MMS-coercive-field H_c^{MMS}, which does not necessarily coincide with the coercive field H_c. At H_c^{MMS} the magnetic-moment distribution achieves the highest out-of-plane

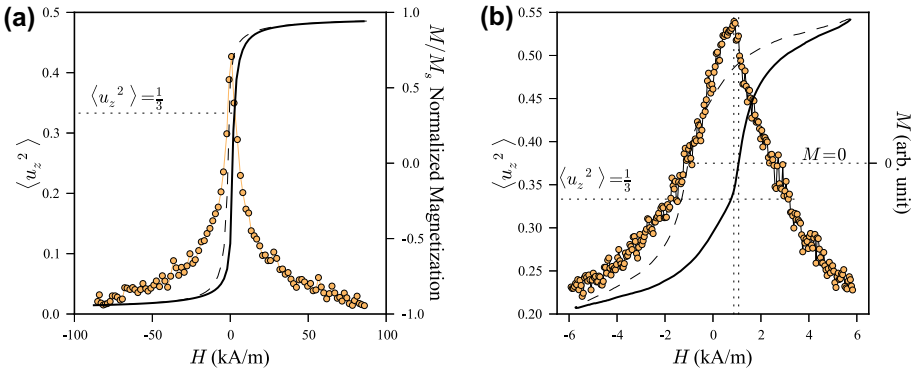

Fig. 4. $\langle u_z^2 \rangle$ vs. applied magnetic field (dots) for the 1 μm sample and M vs. H curves from conventional magnetometric experiments (see Section 3.2 for details). Solid and dash lines stand for M vs. H lower and upper branches respectively. Only the lower branch of the cycle (solid line, $dH/dt > 0$) compares directly with the corresponding $\langle u_z^2 \rangle$ data. (a) $\langle u_z^2 \rangle$ as obtained from MMS curves shown in Fig. 3(e) through Eq. (3). Guideline is at $\langle u_z^2 \rangle = 1/3$. (b) $\langle u_z^2 \rangle$ from MMS experiments performed at lower magnetic-field amplitude (not shown here). Guidelines are at $\langle u_z^2 \rangle = 1/3, M = 0$, magnetic coercive field (right) and MMS coercive field (left).

texture. For higher fields, a continuous diminution of $\langle u_z^2 \rangle$ is observed, in accordance with a magnetization process.

In order to increase the resolution around H_c^{MMS} region, a new set of MMS experiments with alternating magnetic fields of lower amplitude were performed (not shown). In addition, M vs. H cycles were also measured in order to contrast with these MMS results (see Section 3.2 for experimental details). In Fig. 4(b) the $\langle u_z^2 \rangle$ obtained from these new MMS curves through Eq. 3 is compared with the corresponding magnetization cycle. It can be seen the H_c^{MMS} is somehow lower than the coercivity H_c. Consistently with the fact that H_c is the needed field to achieve $\langle u_x \rangle = 0$ while H_c^{MMS} corresponds to the maximum of $\langle u_z^2 \rangle$. Thus, it is apparent that even if both values are intended to indicate the transition from the demagnetization to the magnetization processes, they should not necessarily coincide. The informations obtained from MMS experiments and M vs. H cycles are complementary. For example, it can be assured from the information obtained from both technique that the distribution of magnetic-moments orientations never passes through a random distribution (in which $\langle u_x^2 \rangle = \langle u_y^2 \rangle = \langle u_z^2 \rangle = \frac{1}{3}$ and $\langle u_x \rangle = \langle u_y \rangle = \langle u_z \rangle = 0$), since $\langle u_z^2 \rangle$ equals $\frac{1}{3}$ at a different field value than H_c ($\langle u_x \rangle = 0$).

Note that the $\langle u_z^2 \rangle$ of the low-amplitude MMS experiment (Fig. 4(a)) it is located above the high-amplitude one (Fig. 4(b)). This should not be surprising because they are responses to alternating magnetic fields of different amplitudes. For example, in hysteresis loops low-amplitude cycles (minor cycles) appears inside the high-amplitude cycles. This feature is related to the hysteretic behavior of magnetic cycles originated in the magnetic state dependence on history. In such minor cycles $\langle u_z^2 \rangle$ is expected to be greater than or equal to the corresponding values obtained at a major cycle.

4.2. Thick absorber

For the thicker sample Eq. (2) are not anymore applicable. In fact, even these equations predict critical points common to all the MMS curves (independently of the chosen line), two minima appear in the fifth-line MMS curve around ±15 kA/m (see Fig. 3(f)) which are not present as critical points in the other scans. Thus, it is evident that the simultaneous interpretation of the three curves by the thin-absorber-approximation cannot be done even qualitatively.[1]

[1] A short discussion about this assertion can be found in a previous work, where the same features of the fifth-line MMS curve were observed in a $Fe_{90}Zr_7B_3$ nanocrystalline alloy [13].

The two extra minima appear due to the gamma-ray polarization process as the gamma-ray crosses the absorber, which is enhanced in thick samples. The intensities of the absorption lines depend not only on the relative direction between γ and $\mathbf{m}_n$ but on the polarization state of the γ. For each one of the six transitions, a given polarization state can be absorbed, which also depends on the relative orientation between $\mathbf{m}_n$ and γ. For example, if $\mathbf{m}_n$ and γ are parallels, transitions only occurs for a given circular polarization state (right or left), while if $\mathbf{m}_n$ and γ are perpendicular, only lineal polarized photons are absorbed (parallel or orthogonal to $\mathbf{m}_n$). If the source is not polarized, only the fraction of photons with the corresponding polarization can be absorbed. In this context, for thick samples the γ-beam is polarized as it crosses the absorbent, and therefore polarization becomes part of the absorption process.

The effect of the polarization process on thick samples can be qualitatively estimated by considering a very thick sample at two extreme $\mathbf{m}_n$-orientation distributions: random oriented and equally oriented. For simplicity we will think that the photons can be absorbed only resonantly, i.e we shall not consider the mass absorption (although mass absorption occurs, it is quite constant in the energy range we are considering and independent of the $\mathbf{m}_n$ orientation). For the random distribution all the photons, regardless of its polarization state, are resonantly absorbed, while on the other case only one half of the γ-beam will be absorbed. In both cases, due to high sample thickness, the intensities of the absorption lines will be independent of the transitions, it should be 100% for the six lines in the former case, and 50% for the lines in the latter case. Therefore if the distribution of $\mathbf{m}_n$-orientations change continuously from the random distribution to the single oriented one, a diminution (due to this polarization effect) on the absorption of the six lines is expected.

For intermediate thicknesses, the absorption lines should evolve between the thin and very-thick behaviors. Expressions given in Eq. (2) also indicate a diminution on the intensities of the lines 1, 3, 4 and 6 for the same evolution of the $\mathbf{m}_n$-orientation distribution. However for the lines 2 and 5 those equations predict an increase. Therefore these lines are the ones which can qualitatively present some feature denoting these two competitive process. Then, to analyze the thick sample MMS curves is necessary to take into account the polarization process of the photons in the sample.

5. Formalism

To develop a formalism for MMS curves analysis the gamma ray polarization must be taken into account. A relatively small fraction

of the published works on Mössbauer effect deals with polarization phenomena [29,30,15]. In particular, polarization concepts are essential to analyze Mössbauer experiments carried out with polarized sources [31–33,24,34]. However, it has been shown that using an unpolarized source these concepts may also be important [35]. In fact, as was reported in Ref. [36], incorrect site populations were inferred in some experiments in which polarization effects were left aside in the analysis.

There are various ways to consider polarization in resonant absorption processes [37,25,30]. In this work, we follow and improve a density matrix method, as is presented by Daniels [20] and Hirvonen et al. [19]. In this representation, we define the Mössbauer absorption effect ($\mathrm{ef}(v)$) in a transmission geometry as

$$\mathrm{ef}(v) = 1 - \frac{1}{\pi}\int_{-\infty}^{\infty} \frac{Tr\left\{\rho e^{-t\sum_{i=1} g_i(v;\varepsilon)\sigma_i}\right\}}{1+\varepsilon^2} d\varepsilon, \tag{4}$$

where

- v is the relative velocity between absorber and source.
- $g_i(v;\varepsilon) = \frac{1}{1+(\varepsilon-\varepsilon_i)^2}$ is the ith transition absorption function with $\varepsilon_i = \frac{E_0\left(1+\frac{v}{c}\right)-E_i}{\Gamma/2}$, and being Γ the half-width of the emission (or absorption) profile, E_0 the gamma source transition energy, E_i the ith absorber transition energy and c the light speed in vacuum.
- t is the Mössbauer effective thickness of the absorber.
- ρ is the density matrix of the polarization states (2×2 matrix).
- σ_i is the absorption matrix of the ith transition in the space of polarization states (assumed independent of z).

The absorption matrices depend on the relative orientation between the nuclear spin and the gamma-ray and the spin state mixture of the involved levels. These matrices are hermitian and can be written as

$$\sigma_i = \begin{pmatrix} a_i + b_i & c_i - id_i \\ c_i + id_i & a_i - b_i \end{pmatrix}. \tag{5}$$

Hirvonen et al. [38] calculated these quantities for pure magnetic transitions, for an arbitrary relative orientation between gamma-ray beam and magnetic-moments directions. On the left side of Table 1 the coefficients of the six absorption matrices are listed.

The theoretical absorption spectrum for a sample with a single orientation for all magnetic-moments ($\hat{\mathbf{u}} = (u_x, u_y, u_z)$), is obtained by inserting in Eq. (4) the six σ_i matrices constructed using the values listed in Table 1. In our case the sample presents a distribution of magnetic-moment orientations $\varrho(\vec{r},\Omega)$ (i.e. is not single-oriented). For a homogeneous distribution ($\varrho(\vec{r},\Omega) = \varrho(\Omega)$), Eq. (4) is still valid but with the absorption matrices obtained by averaging the matrices on the orientation distribution:

$$\langle\sigma_i\rangle = \int \varrho(\Omega)\sigma_i(\Omega)d\Omega, \tag{6}$$

which results in,

$$\langle\sigma_i\rangle = \begin{pmatrix} \langle a_i\rangle + \langle b_i\rangle & \langle c_i\rangle - i\langle d_i\rangle \\ \langle c_i\rangle + i\langle d_i\rangle & \langle a_i\rangle - \langle b_i\rangle \end{pmatrix}. \tag{7}$$

If the set of matrices $\langle\sigma_i\rangle$ commute, it is possible to find a polarization basis which diagonalize them all, with their eigenvalues as the diagonal elements. Besides, for non-polarized gamma-ray the density matrix representation is the same whatever basis is chosen: $\rho = \mathrm{diag}\{\frac{1}{2},\frac{1}{2}\}$. Assuming these conditions, Eq. (4) is reduced to,

$$\mathrm{ef}(v) = 1 - \frac{1}{\pi}\int_{-\infty}^{\infty} \frac{1}{1+\varepsilon^2}\left(\frac{1}{2}e^{-t\sum_{i=1} g_i(v;\varepsilon)(\langle a_i\rangle + a_i')} + \frac{1}{2}e^{-t\sum_{i=1} g_i(v;\varepsilon)(\langle a_i\rangle - a_i')}\right) d\varepsilon, \tag{8}$$

where $\langle a_i\rangle + a_i'$ and $\langle a_i\rangle - a_i'$ are the two eigenvalues of $\langle\sigma_i\rangle$, being $a_i' = \sqrt{\langle b_i^2\rangle + \langle c_i^2\rangle + \langle d_i^2\rangle}$.

For a distribution of atomic magnetic-moment orientations with mirror symmetry respect to x-y and x-z planes (see Fig. 2) $\langle u_z\rangle$ and $\langle u_x u_y\rangle$ vanish. Therefore the matrices $\langle\sigma_i\rangle$ become symmetric and commute among them allowing Eq. (8) to be used. Under these conditions, absorption matrices depend only on $\langle u_z^2\rangle$ and $|\langle u_y^2\rangle - \langle u_x^2\rangle|$. On the last two columns of Table 1 $\langle a_i\rangle$ and a_i' for this symmetric case are listed. These two quantities are associated with the out-of-plane component and the in-plane asymmetry of the magnetic-moment orientations distribution respectively.

It should be stressed that Eq. (8) can be easily extended to a sample having an hyperfine magnetic field distribution replacing the Lorentzian absorption probability $g_i(v;\varepsilon)$ by the corresponding probability distribution. Eq. (8) is one of the main results of this paper and should be the starting point for MMS analyses performed on any sample where magnetic-moment orientation distribution is spatially homogeneous with mirror symmetry respect to the x-y and x-z planes.

6. Analysis of thick sample experimental data

Owing to the experimental configuration used in this work (see Fig. 2 keeping in mind the sample symmetry and the symmetry of the magnetic anisotropy distribution), the MMS curve from the 13 μm α-Fe sample can be analyzed assuming valid the magnetic-moment distribution symmetries considered in the previous section.

Table 1
The first four columns are the coefficients of the absorption matrix σ_i (see Eq. 5) for a single-orientation of magnetic-moments given by the unit vector $\hat{\mathbf{u}} = (u_x, u_y, u_z)$. Adapted from Ref. [38] to this work axis-convention: gamma-ray beam in the z direction. The two last columns are related with samples with an homogeneous distribution of atomic moments orientations with symmetries such $\langle u_x u_y\rangle = 0$ and $\langle u_z\rangle = 0$. $\langle a_i\rangle$ and a_i' are related with the eigenvalues $\langle a_i\rangle \pm a_i'$ of the matrix $\langle\sigma_i\rangle$.

Line	Single-orientation				Symmetric multi-orientation	
	a_i	b_i	c_i	d_i	$\langle a_i\rangle$	$a_i' = \sqrt{\langle b\rangle^2 + \langle c\rangle^2 + \langle d\rangle^2}$
1	$\frac{3}{16}(1+u_z^2)$	$-\frac{3}{8}u_z$	$-\frac{3}{16}(u_y^2-u_x^2)$	$\frac{3}{8}u_x u_y$	$\frac{3}{16}(1+\langle u_z^2\rangle)$	$\frac{3}{16}\left\lvert\langle u_y^2\rangle - \langle u_x^2\rangle\right\rvert$
2	$\frac{1}{4}(1-u_z^2)$	0	$\frac{1}{4}(u_y^2-u_x^2)$	$-\frac{1}{2}u_x u_y$	$\frac{1}{4}(1-\langle u_z^2\rangle)$	$\frac{1}{4}\left\lvert\langle u_y^2\rangle - \langle u_x^2\rangle\right\rvert$
3	$\frac{1}{16}(1+u_z^2)$	$\frac{1}{8}u_z$	$-\frac{1}{16}(u_y^2-u_x^2)$	$\frac{1}{8}u_x u_y$	$\frac{1}{16}(1+\langle u_z^2\rangle)$	$\frac{1}{16}\left\lvert\langle u_y^2\rangle - \langle u_x^2\rangle\right\rvert$
4	$\frac{1}{16}(1+u_z^2)$	$-\frac{1}{8}u_z$	$-\frac{1}{16}(u_y^2-u_x^2)$	$\frac{1}{8}u_x u_y$	$\frac{1}{16}(1+\langle u_z^2\rangle)$	$\frac{1}{16}\left\lvert\langle u_y^2\rangle - \langle u_x^2\rangle\right\rvert$
5	$\frac{1}{4}(1-u_z^2)$	0	$\frac{1}{4}(u_y^2-u_x^2)$	$-\frac{1}{2}u_x u_y$	$\frac{1}{4}(1-\langle u_z^2\rangle)$	$\frac{1}{4}\left\lvert\langle u_y^2\rangle - \langle u_x^2\rangle\right\rvert$
6	$\frac{3}{16}(1+u_z^2)$	$\frac{3}{8}u_z$	$-\frac{3}{16}(u_y^2-u_x^2)$	$\frac{3}{8}u_x u_y$	$\frac{3}{16}(1+\langle u_z^2\rangle)$	$\frac{3}{16}\left\lvert\langle u_y^2\rangle - \langle u_x^2\rangle\right\rvert$

When there is no overlapping of the absorption lines, as in our case, it is possible to obtain an analytical expression for the Mössbauer effect in terms of Bessel functions at the center of each line [14]. So, the ith line Mössbauer effect becomes,

$$\mathrm{ef}_i = 1 - \frac{1}{2}e^{-\frac{t}{2}(\langle a_i\rangle + a_i')} I_0\left(\frac{t}{2}(\langle a_i\rangle + a_i')\right) - \frac{1}{2}e^{-\frac{t}{2}(\langle a_i\rangle - a_i')} I_0\left(\frac{t}{2}(\langle a_i\rangle - a_i')\right), \tag{9}$$

where I_0 is the zero-order modified Bessel function.

Consequently, we are able to obtain the dependences of $\langle u_z^2\rangle$ and $|\langle u_y^2\rangle - \langle u_x^2\rangle|$ on the applied magnetic field using Eq. (9). Since line 1 is equivalent to line 6, 2 equivalent to 5, and 3 to 4; the three MMS curves shown in Fig. 3(f) are a complete set of independent scans. The measured normalized transmission $Y_{i,j}$ for the ith line at a given applied field H_j is linked to $\langle u_z^2\rangle$ and $|\langle u_y^2\rangle - \langle u_x^2\rangle|$ by,

$$\mathrm{ef}_i\left(t, \langle u_z^2\rangle_j, |\langle u_y^2\rangle - \langle u_x^2\rangle|_j\right) \approx \frac{(1 - Y_{ij})}{\beta}, \tag{10}$$

where $\beta < 1$ is a factor which takes into account spurious radiation coming from other sources than the 14.4 keV of the ^{57}Fe nuclear transition (such as Compton scattering coming from photons of higher transitions of the Mössbauer source). The dependence of ef_i on $\langle u_z^2\rangle$ and $|\langle u_y^2\rangle - \langle u_x^2\rangle|$ is given by $\langle a_i\rangle$ and a_i'. The symbol ($\approx$) is used to emphasize the fact that, because of the experimental data dispersion, the equations will never be exactly satisfied.

For each point of each MMS curves, an implicit equation for $\langle u_z^2\rangle_j$ and $|\langle u_y^2\rangle - \langle u_x^2\rangle|_j$ is obtained through Eq. (10). Then for each H_j there are three equations and four unknowns: $t, \beta, \langle u_z^2\rangle_j$ and $|\langle u_y^2\rangle - \langle u_x^2\rangle|_j$. Being N different H_j, a system of $3N$ equations with $2N+2$ unknowns is finally obtained. The existence of a solution to the equations system is an indication of the mathematical model goodness. But the finding of such solution is frustrated by the experimental dispersion of the data, eliminating the possibility of finding a unique and exact solution. So only a *best* set of values for the unknowns can be found. We used as a measure of the goodness of the values the expression:

$$\sum_{i=\{3,5,6\}}\sum_{j=1}^{N}\left[\frac{1 - Y_{ij}}{\beta} - \mathrm{ef}_i\left(t, \langle u_z^2\rangle_j, |\langle u_x^2\rangle - \langle u_y^2\rangle|_j\right)\right]^2, \tag{11}$$

being the best set of values the one that minimize it. The NMINIMIZE routine of the MATHEMATICA software was used to search for the global minimum of the last expression. It must be emphasized that this procedure is different from a curve fitting method. In the present case no model is proposed for the dependence of $\langle u_z^2\rangle$ and $|\langle u_x^2\rangle - \langle u_y^2\rangle|$ on the applied magnetic field. They are obtained independently for each applied field, the only common unknowns for all equations are the effective thickness t and the β factor.

The corresponding minimization over the MMS curves from the 13 μm sample gives $\beta = 0.440(4)$ and $t = 3.25(3)$. [2] The attained set of $\langle u_z^2\rangle$ and $|\langle u_x^2\rangle - \langle u_y^2\rangle|$ values are plotted in Fig. 5 as a function of the applied magnetic field. As can be observed, both quantities have the expected dependencies: as the field increases the out-of-plane projection of the magnetic-moment orientation distribution goes to zero, while the asymmetry on the sample plane (x-y) goes to its maximum value. The asymmetry $|\langle u_x^2\rangle - \langle u_y^2\rangle|$ increases for increasing field because $\langle u_x^2\rangle$ grows at expenses of $\langle u_y^2\rangle$ (remember that the field is applied in the x-direction, Fig. 2). The goodness of the minimization process can be appreciated in Fig. 6 by comparing the experimental curves with those calculated from Eq. (9) by using the obtained set of $\langle u_z^2\rangle$ and $|\langle u_x^2\rangle - \langle u_y^2\rangle|$ values.

[2] The error on each variable (one standard deviation) was determined using the statistical F-test following Ref. [39].

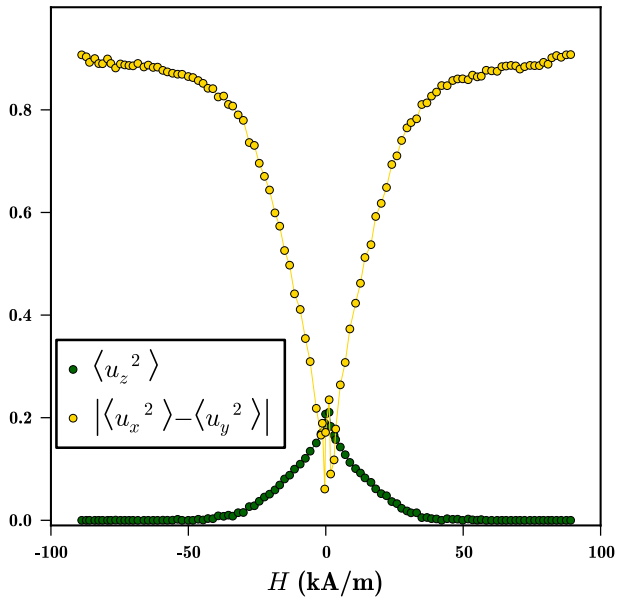

Fig. 5. $\langle u_z^2\rangle$ and $|\langle u_x^2\rangle - \langle u_y^2\rangle|$ of the 13 μm sample. Obtained from the minimization analysis done over the MMS curves.

The two in-sample-plane projections can be isolated considering that the three second-order-moments of the orientation distribution add to one:

$$\langle u_x^2\rangle = \frac{1 - \langle u_z^2\rangle \pm |\langle u_x^2\rangle - \langle u_y^2\rangle|}{2}, \tag{12a}$$

$$\langle u_y^2\rangle = \frac{1 - \langle u_z^2\rangle \mp |\langle u_x^2\rangle - \langle u_y^2\rangle|}{2}. \tag{12b}$$

The sign ambiguity is due to the absolute value, but only one solution is relevant. This ambiguity can be eliminated by ensuring a

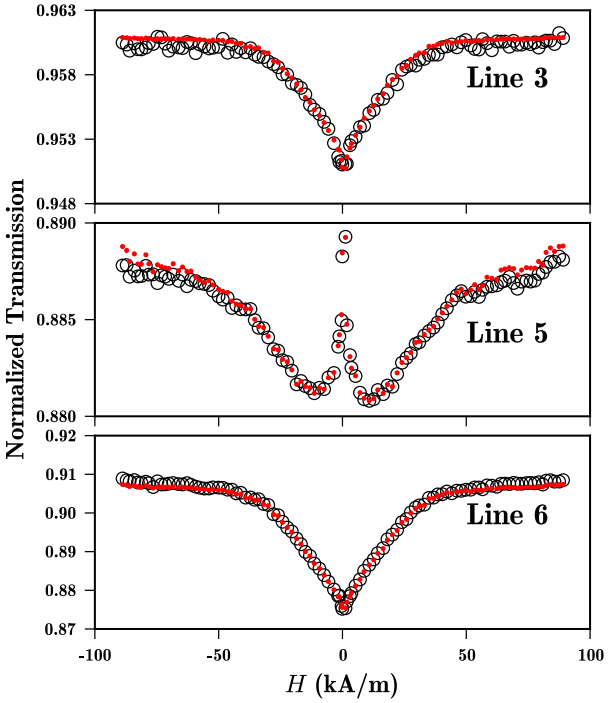

Fig. 6. MMS curves (open dots) of the 13 μm sample (same curves plotted in Fig. 3 (f)) compared with calculated scans (closed dots) provided by Eq. (9) and the parameters given by the minimization analysis (shown in Fig. 5).

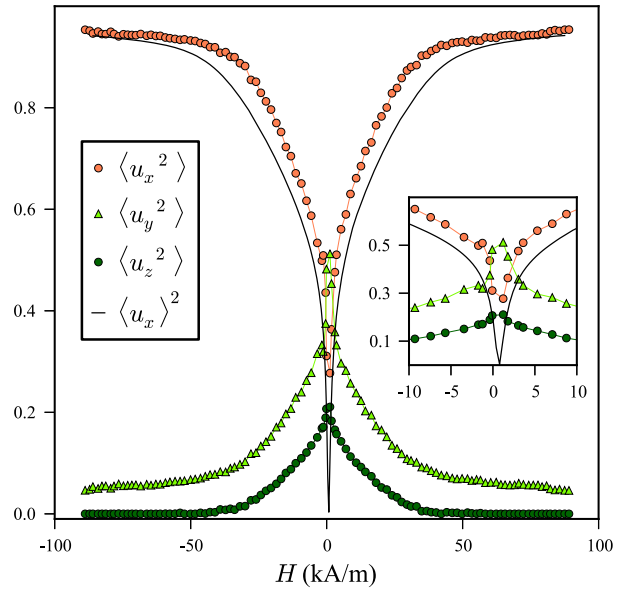

Fig. 7. (Color online) Field dependence of the three second-order-moments of the magnetic-moment orientation distribution for the α-Fe 13 μm sample. The solid black curve correspond to $\langle u_x \rangle^2$ obtained from VSM measurements.

high-field limit for $\langle u_x^2 \rangle$ and $\langle u_y^2 \rangle$ of one and zero respectively, and requesting continuity in the low field region. Henceforth, values of the three mean-square-projection on all applied-magnetic-field range can be retrieved (Fig. 7).

From this results a continuous variation of the magnetic-moment distribution towards saturation is inferred. From the Fig. 7 curves it can be concluded that all the magnetic-moments are in the sample plane for fields higher than 35 kA/m. This small field is enough to completely turn the magnetic-moments onto the sample plane. For higher fields, the magnetization process takes place only within the sample plane, continuously reducing $\langle u_y^2 \rangle$ and increasing $\langle u_x^2 \rangle$. In the demagnetization process (which starts at the most negative field, −90 kA/m), initially the magnetic-moments remain on the sample plane, i.e the $\langle u_z^2 \rangle$ is zero while $\langle u_x^2 \rangle$ and $\langle u_y^2 \rangle$ monotonously decrease and increase, respectively. The out of plane component becomes appreciable at about −35 kA/m. The highest dispersion in the z-direction is achieved at H_c^{MMS} (0.55 kA/m) in which $\langle u_z^2 \rangle = 0.22$, $\langle u_y^2 \rangle = 0.54$ and $\langle u_x^2 \rangle = 0.25$.

As for the thin sample, a M vs. H cycle was measured under conditions equivalents to those of the MMS experiments (VSM measurement, see Section 3.2 for more details). The normalized magnetization M/M_s (where M_s is the saturation magnetization) on the x direction is related to the first order moment $\langle u_x \rangle$ of the orientation distribution of the magnetic-moments. The square of this moment is related to the second-order moment $\langle u_x^2 \rangle$ through the variance of u_x,

$$Var[u_x] = \langle u_x^2 \rangle - \langle u_x \rangle^2 \geqslant 0 \tag{13}$$

In Fig. 7 (black line) the $\langle u_x \rangle^2 = (M/M_s)^2$ curve is plotted. A good agreement with MMS curves is observed: $\langle u_x \rangle^2$ is lower than $\langle u_x^2 \rangle$ as the inequality Eq. 13 holds. Furthermore, in both experiments three common regions of high, medium and low slopes can be recognized. Also, H_c and H_c^{MMS} are very similar, which means that the magnetic-moments in the magnetic cycle passes through the most z-dispersed distribution at the same field at which the x-magnetization passes through its zero value. As was stated for the thin-sample case, the non coincidence between the field at which $M = 0$ and $\langle u_z^2 \rangle = \frac{1}{3}$ indicates that an isotropic state does not appear in the evolution of the orientation distribution. The same conclusion can be deduced exclusively from the MMS curves, since the three second order moments are never simultaneously equal to $\frac{1}{3}$.

7. Discussion

To illustrate and provide a deeper understanding of the MMS technique we compare the magnetic behavior of both samples. As their thickness differ markedly and they were produced using quite different preparation techniques, distinct magnetic behaviors are expected. The 13 μm sample is a commercially available Mössbauer calibration foil produced by lamination and a subsequent annealing treatment in order to eliminate defects, whereas the 1 μm sample was prepared by deposition of sputtered iron onto a Kapton substrate at 373 K.

The $\langle u_x \rangle$ vs. H cycles obtained by vibrating sample magnetometry (VSM) are shown in Fig. 8(a) for both samples (note that $\langle u_x \rangle = M/M_s$). It can be seen that the 13 μm sample is magnetically softer than the 1 μm one: it displays a slightly lower coercive field and has a maximum magnetization closer to the saturation value.

The MMS results provide information about the mean quadratic projections. In Fig. 8(b) it is clear that $\langle u_z^2 \rangle$ is larger for the thin sample than for the thick one in the whole range of applied fields. Hence the thin sample has a larger out-of-plane anisotropy than the thick one. This conclusion is consistent with the fact that at low-field, $\langle u_z^2 \rangle$ takes values which are larger and smaller than those expected for a uniform distribution of magnetic moments for the

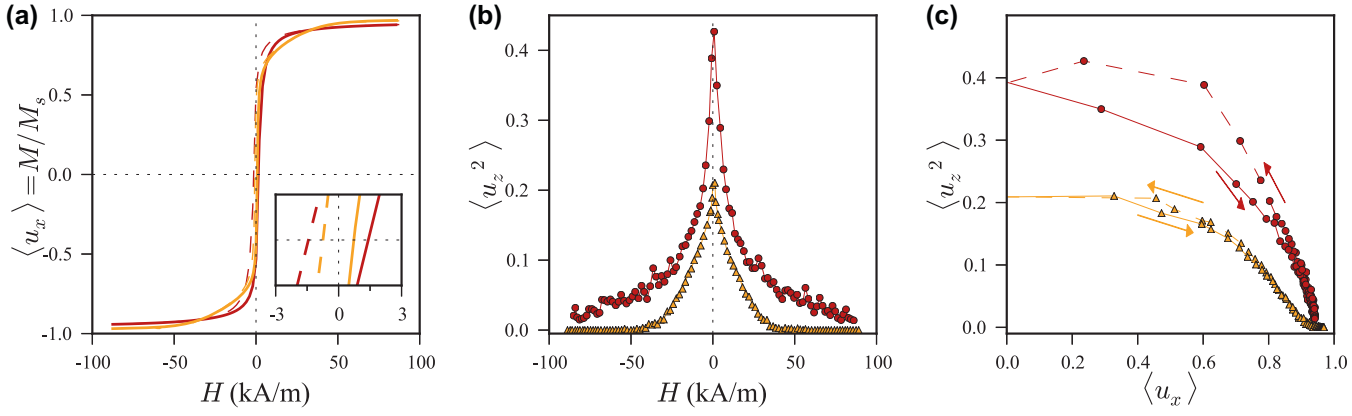

Fig. 8. (a) M vs. H curves, dark line (red) for 1 μm sample and light line (yellow) for 13 μm sample. (b) $\langle u_z^2 \rangle$ vs. H and (c) $\langle u_z^2 \rangle$ vs. $\langle u_x \rangle$, dark circles for the 1 μm sample and light triangles for the 13 μm sample. Solid and dash curves correspond to $dH/dt > 0$ and $dH/dt < 0$ branches. (For interpretation of the references to color in this figure caption, the reader is referred to the web version of this article.)

thin and thick samples, respectively. Therefore the thin sample presents a preferential out-of-plane anisotropy whereas the thick one presents a preferential in-plane anisotropy. The MMS results confirm the softer behavior of the thick sample: the H_c^{MMS} is smaller than that of the thin sample and, within the range of fields investigated, $\langle u_z^2 \rangle$ reaches a null value for the thick sample (at about 35 kA/m) while this does not occur for the thin sample.

The preference observed in anisotropy may be related to surface to volume ratio and to stress. For the thin sample the out-of-plane preference may be due to the stresses originated in the sample cooling to room temperature [40] after the sputtering procedure. As Kapton thermal coefficient of linear expansion (~20 ppm/K) is higher than iron one (~11 ppm/K), the cooling process induce compression stresses on the iron film. Thus, due to positive magnetostriction an effective enhancement of the out-of-plane anisotropy is expected. On the other hand, for the thick sample fabrication process and sample shape favor in-plane anisotropy.

From the combination of VSM ($\langle u_x \rangle$ vs. H) and MMS ($\langle u_z^2 \rangle$ vs. H) measurements the path that the moment distribution follows in the space $(\langle u_x \rangle, \langle u_z^2 \rangle)$ can be obtained. The corresponding curves are shown in Fig. 8(c). This representation allows the study of the distribution of magnetic moments and its evolution towards magnetic saturation independently of H. It can be observed that the thin sample follows a path of larger dispersion in z than the thick one.

8. Conclusions

In the present work a new experimental technique for magnetic characterization of soft magnetic materials is introduced. Using the ^{57}Fe 14.4 keV nuclear transition, the dependence of the magnetic atomic moments orientations on an external field has been studied by performing MMS experiments, i.e. by recording the magnetic field dependence of the nuclear resonant absorption at a constant Doppler energy. MMS curves acquired on thin and thick absorbers differ remarkably at lines 2 and 5 of their magnetically split spectrum, due to the gradual polarization that the gamma-ray, emitted by the unpolarized source, as it travels through the sample.

The polarization effect was successfully taken into account for MMS data analysis using the density matrix formalism. All the registered MMS curves were quantitatively reproduced. Although data treatment is more complex for thick absorbers than for thin ones, it allows the retrieval of more information. The dependence on the applied magnetic field of the three second-order moments of the atomic magnetic-moment orientation distribution was obtained from three independent MMS curves in the case of thick sample. MMS experiments complement and enhance information obtained from other techniques, like magnetometry which provides only information on the first-order moment. The present work brings some examples of this complementarity by revealing the path of the magnetic distribution in the space $(\langle u_x \rangle, \langle u_z^2 \rangle)$ for two model samples. The existence of a strong out-of-plane anisotropy for the thin sample and in-plane anisotropy for the thick sample are reveled. The short range order sensitivity of the Mössbauer effect combined with the constant velocity mode approach can be used for observing distinctive field dependences of magnetic-moments located at non equivalent sites of a given substance, or at different phases of a composite system, by performing MMS experiments at conveniently chosen Doppler energies.

Acknowledgments

This work was financially supported by CONICET and ANPCyT of Argentina, through PIP 6011 and PICT 12-14526. We are grateful to Ing. Nolberto Martínez, who passed away during the preparation of this paper, for the useful discussions we held on the topic, and his insightful contributions, and to Dr. Elisa M. Baggio Saitovitch of CBPF where the 1 μm sample was prepared.

References

[1] J. Stöhr, Exploring the microscopic origin of magnetic anisotropies with x-ray magnetic circular dichroism (xmcd) spectroscopy, J. Magn. Magn. Mater. 200 (1999) 470–497.
[2] J. Dreiser, K.S. Pedersen, T. Birk, M. Schau-Magnussen, C. Piamonteze, S. Rusponi, T. Weyhermüller, H. Brune, F. Nolting, J. Bendix, X-ray magnetic circular dichroism (xmcd) study of a methoxide-bridged dyiii–criii cluster obtained by fluoride abstraction from cis-criiif2(phen)2+, J. Phys. Chem. A 116 (2012) 7842–7847.
[3] A. Cady, D. Haskel, J.C. Lang, Z. Islam, G. Srajer, A. Ankudinov, G. Subías, J. García, Site-specific magnetization reversal studies of magnetite, Phys. Rev. B 73 (2006) 144416.
[4] N. Greenwood, T. Gibb, Mössbauer Spectroscopy, Chapman and Hall, 1971.
[5] D. Dickson, F. Berry, Mössbauer Spectroscopy, Cambridge University Press, Berry, 2005.
[6] Y. Yoshida (Ed.), Proceedings of the 31st International Conference on the Applications of the Mössbauer Effect (ICAME 2011) Tokyo, Japan, 2011, Springer, Netherlands, 2012.
[7] R.S. Preston, S.S. Hanna, J. Heberle, Mössbauer effect in metallic iron, Phys. Rev. 128 (1962) 2207–2218.
[8] C.L. Chien, Mössbauer study of a binary amorphous ferromagnet: Fe80B20, Phys. Rev. B 18 (1978) 1003–1015.
[9] H.E. Marcolin, R. Rescheke, A. Trautwein, Mössbauer spectroscopic investigations of photodissociated myoglobin-co at low temperatures, Eur. J. Biochem. 96 (1979) 119–123.
[10] F. Sánchez, G. Pasquevich, P. Mendoza Zélis, F.A. Cabrera, L. Ying feng, M. van Fernández, Study of magnetic materials by Mössbauer thermal scans. Application to nanocrystalline systems, J. Methods Nanocryst. Mater. 22 (2004) 39.
[11] P. Mendoza Zélis, G. Pasquevich, F. Sánchez, N. Martínez, A. Veiga, A new application of Mössbauer effect thermal scans: determination of the magnetic hyperfine field temperature dependence, Phys. Lett. A 298 (2002) 55–59.
[12] P. Mendoza Zélis, G. Pasquevich, A. Veiga, M. Fernández van Raap, F. Sánchez, A quasi-continuous observation of the -transition of fe1+xs by Mössbauer line tracking, Hyperfine Interact. 195 (2010) 161–165.
[13] G. Pasquevich, P. Mendoza Zélis, F. Sánchez, M. Fernández van Raap, A. Veiga, N. Martínez, Determination of the iron atomic magnetic moments dynamics in the nanocrystalline ribbons fe90zr7b3 by Mössbauer magnetic scans, Phys. B (Amsterdam, Neth.) 384 (2006) 348–350.
[14] S. Margulies, J. Ehrman, Transmission and line broadening of resonance radiation incident on a resonance absorber, Nucl. Instrum. Methods 12 (1961) 131–137.
[15] J.M. Williams, J.S. Brooks, The thickness dependence of Mössbauer absorption line areas in unpolarized and polarized absorbers, Nucl. Instrum. Methods 128 (1975) 363–372.
[16] U. Gonser, F. Aubertin, S. Stenger, H. Fischer, G. Smirnov, G. Klingelhöfer, Polarization and thickness effects in Mössbauer spectroscopy, Hyperfine Interactions 67 (1991) 701–709.
[17] D. Rancourt, Accurate site populations from Mössbauer spectroscopy, Nucl. Instrum. Methods Phys. Res. Sec. B: Beam Interact. Mater. Atoms 44 (1989) 199–210.
[18] U. Gonser, H. Fischer, $\alpha-^{57}$ Fe spectra only, Hyperfine Interact. 72 (1992) 31–44.
[19] M.T. Hirvonen, T. Katila, K. Riski, J. Tanttu, Transmission of polarized rays in a medium with anisotropic nuclear resonance absorption, Phys. Rev. B 24 (1981) 11–16.
[20] J. Daniels, The interpretation of Mössbauer spectra obtained with polarized gamma-rays and single crystal absorbers, Nucl. Instrum. Methods 128 (1975) 483–493.
[21] B. Fultz, Mössbauer Spectrometry, Characterization of Materials, John Wiley, New York, 2011.
[22] H. Pfannes, H. Fischer, The texture problem in Mössbauer spectroscopy, Appl. Phys. 13 (1977) 317–325.
[23] J. Greneche, F. Varret, On the texture problem in Mössbauer spectroscopy, J. Phys. C: Solid State Phys. 15 (1982) 5333–5344.
[24] K. Szymański, Polarized radiation in Mössbauer spectroscopy, Phys. Rep. 423 (2006) 295–338.
[25] R. Nussbaum, R. Housley, Internal conversion in fe57 from the Mössbauer effect in iron, Nucl. Phys. 68 (1965) 145–152.
[26] A. Veiga, N. Martínez, P. Mendoza Zélis, G. Pasquevich, F. Sánchez, Advances in constant-velocity Mössbauer instrumentation, Hyperfine Interact. 167 (2006) 905–909.
[27] A. Veiga, G. Pasquevich, P. Mendoza, F. Sánchez, M. Fernández van Raap, N. Martínez, Experimental design and methodology for a new Mössbauer scan experiment: absorption line tracking, Hyperfine Interact. 188 (2009) 137–142.
[28] E. du Trémolet de Lacheisserie, D. Gignoux, M. Schlenker, Magnetism: Fundamentals, Magnetism, vol. 1, 2005.
[29] S.S. Hanna, R.S. Preston, Mössbauer cross section of 57Fe in iron, Phys. Rev. 139 (1965) A722–A725.

[30] R.M. Housley, R.W. Grant, U. Gonser, Coherence and polarization effects in Mössbauer absorption by single crystals, Phys. Rev. 178 (1969) 514–522.
[31] U. Gonser, M. Ghafari, H. Wagner, H. Fischer, Spin texture determination in amorphous Fe80B20 by linearly polarized recoil-free -rays, J. Phys. Colloque C2 (40) (1979) 126.
[32] W. Olszewski, K. Szymański, D. Satula, L. Dobrzyński, Magnetic texture determination by CEMS with polarized radiation, Nukleonika 52 (2007) S17.
[33] K. Szymański, Evaluation of Mössbauer spectra measured by monochromatic, circularly polarised radiation, Nucl. Instrum. Methods Phys. Res., Sect. B 168 (2000) 125–132.
[34] F. Tanczikó, L. Bottyán, L. Deák, D. Merkel, D. Nagy, Sign determination of the hyperfine field by elliptically polarized Mössbauer source, Hyperfine Interact. 188 (2009) 79–84.
[35] U. Gonser, H. Fischer, Mössbauer dichroism, Hyperfine Interact. 26 (1985) 845–853.
[36] R.M. Housley, U. Gonser, R.W. Grant, Mössbauer determination of the Debye–Waller factor in single-crystal absorbers, Phys. Rev. Lett. 20 (1968) 1279–1282.
[37] H. Frauenfelder, D.E. Nagle, R.D. Taylor, D.R.F. Cochran, W.M. Visscher, Elliptical polarization of Fe^{57} gamma rays, Phys. Rev. 126 (1962) 1065–1075.
[38] M.T. Hirvonen, Theory of polarimetric resonance electron Mössbauer spectroscopy, Nucl. Instrum. Methods 165 (1979) 67–82.
[39] R. Gill, Gamma-ray angular correlations, Academic Press, 1975.
[40] P. Mendoza Zélis, F.H. Sánchez, M. Vázquez, Magnetostrictive bimagnetic trilayer ribbons for temperature sensing, J. Appl. Phys. 101 (2007) 034507.